

Anisotropic Fracture of Graphene Revealed by Surface Steps on Graphite


Cangyu Qu^{1,*}, Diwei Shi^{2,3}, Li Chen^{2,3}, Zhanghui Wu^{2,3}, Jin Wang^{2,3}, Songlin Shi^{2,3},
Enlai Gao⁴, Zhiping Xu^{2,3} and Quanshui Zheng^{1,2,3,†}

¹*Institute of Superlubricity Technology, Research Institute of Tsinghua University in Shenzhen, Shenzhen 518057, China*

²*Center for Nano and Micro Mechanics, Tsinghua University, Beijing 100084, China*

³*Department of Engineering Mechanics, Tsinghua University, Beijing 100084, China*

⁴*Department of Engineering Mechanics, School of Civil Engineering, Wuhan University, Wuhan, Hubei 430072, China*

 (Received 27 March 2022; revised 6 June 2022; accepted 13 June 2022; published 6 July 2022)

The anisotropic fracture toughness $G(\theta)$ is an intrinsic feature of graphene and is fundamental for fabrication, functioning, and robustness of graphene-based devices. However, existing results show significant discrepancies on the anisotropic factor, i.e., the ratio between zigzag (ZZ) and armchair (AC) directions, G_{ZZ}/G_{AC} , both qualitatively and quantitatively. Here, we investigate the anisotropic fracture of graphene by atomic steps on cleaved graphite surfaces. Depending on the relation between the peeling direction and local lattice orientation, two categories of steps with different structures and behaviors are observed. In one category are straight steps well aligned with local ZZ directions, while in the other are steps consisting of nanoscale ZZ and AC segments. Combined with an analysis on fracture mechanics, the microscale morphology of steps and statistics of their directions provides a measurement on the anisotropic factor of $G_{ZZ}/G_{AC} = 0.971$, suggesting that the ZZ direction has a slightly lower fracture toughness. The results provide an experimental benchmark for the widely scattered existing results, and offer constraints on future models of graphene fracture.

DOI: [10.1103/PhysRevLett.129.026101](https://doi.org/10.1103/PhysRevLett.129.026101)

Anisotropic fracture toughness is an intrinsic feature of crystals. It has important implications for cleavage or growth of crystals with selective surface orientations. Graphene as a two-dimensional (2D) material has received intensive attention in the past decades for its exceptional properties and promising application potentials [1–5]. Its in-plane fracture is anisotropic, featured by an anisotropic fracture toughness. This fundamental material property is important for the fabrication (e.g., mechanical exfoliation) and robustness (e.g., under high stress) of graphene-based devices, such as, in particular, nanomechanical systems, stretchable electronics, and nanocomposites [6–10]. Evidence suggests that two directions in the graphene lattice, i.e., zigzag (ZZ) and armchair (AC) directions, are preferred for cracks to propagate along. The selection of crack path and direction on the nanoscale can have great impacts on the material's mesoscopic properties [11], and for graphene, it results in ZZ or AC edges with completely different electronic and magnetic properties [12]. These edge-dependent properties are crucial for next-generation electronics based on graphene nanostructures such as nanoribbons [13–16].

Despite its importance, fundamental questions regarding graphene's fracture, such as which of the ZZ and AC directions has the smaller toughness, remain unclear, let alone a quantitative measurement on the anisotropic factor. The fracture toughness, defined as the resistance against the propagation of an initial crack (i.e., critical energy release

rate), is determined by the edge energy of graphene, according to Griffith's theory of brittle fracture [5,17]. Calculations have been performed on graphene's edge energy, or directly on its crack path during fracture. Some existing results indicate that ZZ cracks are more favorable, while others show exactly the opposite [5,18–29]. Even first-principles calculations based on density functional theory are dependent on the methodology such as the exchange-correlation functions and edge structures [22,24]. The same discrepancy applies to experiments, where most observations show similar abundance in ZZ and AC cracks [30–33], while a few report that either AC or ZZ direction is preferred over the other [26,34–38]. Direct measurements on the strength of graphene so far lack reference to the fracture direction [3,5]. Therefore, the fracture anisotropic factor is not resolved. A simple method that is angular sensitive and allows for nanoscale characterization of crack path is needed to gain better insight into nanoscale fracture mechanics.

Mechanical exfoliation is one of the most popular methods to fabricate 2D materials. For graphene, the exfoliation leaves an enormous number of atomic steps on the cleaved graphite surface as a result of mode III fracture of graphene [39–44]. In this Letter, we show that these surface steps contain valuable information on the fracture properties of graphene. Using a high-resolution atomic force microscope (AFM), two categories of steps are observed. In one category are groups of parallel steps

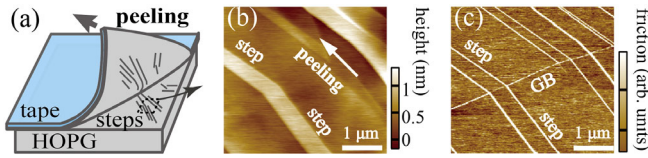


FIG. 1. Experimental setup and AFM images. (a) Top layers of graphite are exfoliated from an HOPG sample with a tape, exposing a cleaved graphite surface with atomic steps. (b) AFM height image. Groups of parallel steps form acute angles with the peeling direction (white arrow). (c) Corresponding friction image. Steps appear as bright (high frictional) lines. A grain boundary (GB) is also found. The steps cross the grain boundary and deflect at the grain boundary due to the change of local lattice orientation.

well aligned with the local ZZ directions. Meanwhile, in the other category are steps consisting of nanoscale ZZ and AC segments. Combining a simple mechanics model with the statistics of step directions, we measure the anisotropic factor for fracture toughness as $G_{ZZ}/G_{AC} = 0.971$. The results suggest that the ZZ direction has a slightly lower fracture toughness, or equivalently, edge energy. They provide an experimental benchmark for the widely scattered existing results, and offer constraints on future theoretical models on graphene fracture.

Conventional mechanical exfoliation (Supplemental Material, Sec. 1) [45] of a polycrystalline graphite sample (highly oriented pyrolytic graphite, HOPG) by a tape (3M, Scotch 810) was carried out, as sketched in Fig. 1(a). The cleaved graphite surface was then characterized by an AFM (Cypher ES, Asylum Research) in lateral force mode. Height and friction images are shown in Figs. 1(b) and 1(c). Surface steps with a typical height of 1 nm (Supplemental Material, Sec. 2) are evident in both height and friction images, as abrupt changes of height, and bright (high frictional) lines, respectively. A grain boundary (GB) is also observed in Fig. 1(c) as a high frictional line, however, with no corresponding height change, which distinguishes itself from a step [48]. Two adjacent grains are divided by this GB. The steps form acute angles with the peeling direction [white arrow in Fig. 1(b)], and they change direction when crossing the GB, due to the change of lattice orientation. This observation provides intuitive evidence that the fracture properties of graphene must be anisotropic, and the steps are following some certain lattice orientations.

Thanks to the high spatial resolution of AFM, when the scan size is reduced to a few nanometers, the graphite lattice can be imaged. The high-resolution lattice images are then used to measure the local lattice orientation at any given position on the graphite surface (Supplemental Material, Sec. 1). Figure 2(a) shows a friction image of an area covering four polygon-shaped grains. Steps are found in the up-down direction, crossing multiple grains. For grains 1–3, the steps form parallel groups within each

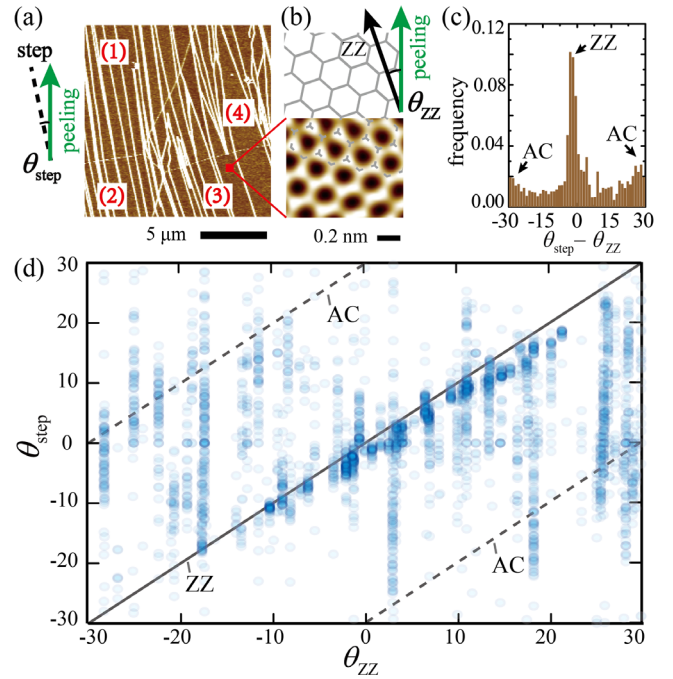


FIG. 2. Statistics of step directions. (a) Friction image of an area covering four grains. θ_{step} is defined as the angle between a given step and the peeling direction (green arrow). (b) High-resolution image showing graphene lattice. The zigzag (ZZ) direction is indicated by the black arrow. θ_{ZZ} is defined as the angle between the ZZ direction and the peeling direction. (c) Histogram of $\theta_{\text{step}} - \theta_{ZZ}$ for data of 3047 steps found in 107 different grains on the HOPG surface. A primary peak at ZZ direction and two secondary peaks at AC directions are found, with a ZZ-to-AC peak height ratio of 4.3. (d) θ_{step} vs θ_{ZZ} plot. A considerable number of data points are clustered near the line of $\theta_{\text{step}} = \theta_{ZZ}$ (i.e., ZZ direction). Meanwhile, the other data points are scattered.

grain and are aligned with the local ZZ directions. As an example, the lattice image that reveals the local ZZ direction for grain 3 is shown in Fig. 2(b). Differently, the steps in grain 4 are not parallel to each other and their directions show large irregularity. For any given step, its direction is quantitatively measured by defining θ_{step} as the angle between the step and the peeling direction. And the local lattice orientation is measured by defining the ZZ angle θ_{ZZ} as the angle between the local ZZ direction and the peeling direction, as sketched in Fig. 2(b). Because of the sixfold symmetry, θ_{ZZ} is in the range of -30° to 30° . Similar imaging and measurements of θ_{step} and θ_{ZZ} were carried out for 3047 steps found in 107 grains on the HOPG surface at 25 different imaged regions, with the results plotted in Figs. 2(c) and 2(d). In the histogram for $\theta_{\text{step}} - \theta_{ZZ}$, Fig. 2(c), a primary peak is found at the ZZ direction ($\theta_{\text{step}} = \theta_{ZZ}$) along with two secondary peaks at AC directions ($\theta_{\text{step}} = \theta_{ZZ} \pm 30^\circ$). The ZZ-to-AC peak height ratio is around 4.3. Meanwhile, Fig. 2(d) further shows that a large number of data points (that is, data for

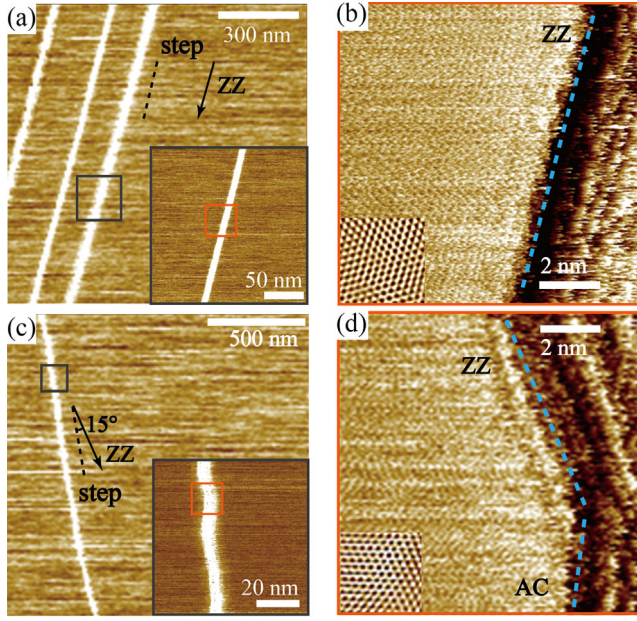


FIG. 3. High-resolution imaging of surface steps. (a) Friction image of an area with three parallel steps. The steps are well aligned with the local ZZ direction (black arrow). The inset shows the close-up image of the black box. (b) Atomic scale image of the orange box in the inset of (a). An atomically sharp and straight ZZ step is clearly observed. The inset shows the filtered image where graphene lattice is better seen. (c) Friction image of an area with a surface step, whose direction (dashed lines) is 15° away from the local ZZ direction (black arrow). The inset shows the close-up image of the black box, where the apparently straight step is revealed to consist of nanoscale segments whose direction can be different from the apparent step direction. (d) Atomic scale image of the orange box in the inset of (c), where a corner connecting a ZZ segment and an AC one is shown.

48 grains out of 107 grains in total) are clustered on the line of $\theta_{\text{step}} = \theta_{\text{ZZ}}$, indicating that these steps are all aligned with the local ZZ directions, while the other data points are significantly scattered.

To understand why some of the steps show a clear trend of following local ZZ directions while others do not, the topography of steps is characterized from microscale down to atomic resolution. Figure 3(a) shows the friction image of a region containing three parallel steps whose directions (dashed lines) are well aligned with the local ZZ direction (black arrow), with the inset showing a close-up image of the black box. A high-resolution scan of one step, as shown in Fig. 3(b), reveals that this ZZ step is atomically sharp and straight. The inset shows the filtered image where the graphene lattice is clearly seen. However, for steps that do not follow local ZZ directions, a completely different picture is found on the nanoscale. Such an example is shown in Fig. 3(c), where the direction of the step is 15° away from the local ZZ direction. A close-up image reveals that the step is not straight but consists of nanoscale segments. This structure implies an oscillation during crack

propagation. Figure 3(d) shows the high-resolution image of a corner on this step where a ZZ segment is connected to an AC one. This observation explains the large irregularity for the scattered data points in Fig. 2(d). For these steps, θ_{step} only represents the apparent step direction on the microscale, and can differ significantly from the directions of the nanoscale segments that are either along ZZ or AC directions. As a result, the apparent step direction does not necessarily follow local ZZ or AC directions, and can have large deviations.

To model the fracture of graphene during exfoliation, we consider that a thin film of graphite is first adhered to the tape. The adhered graphite film as well as the tape undergoes elastic tension and bending due to the peeling loading. This stored strain energy is partially relaxed when the graphene crack advances. However, an energy cost is also associated with this crack extension due to the in-plane fracture of graphene as well as the out-of-plane cleavage of graphite. Considering the three terms, the total energy of the system is [39]

$$U = U_e + 2\gamma st/d + \tau Bl, \quad (1)$$

where U_e is the elastic energy, γ is the graphene edge energy density which is a function of $\theta = \theta_{\text{step}} - \theta_{\text{ZZ}}$, s is the crack length, t/d is the number of fractured graphene layers, with t and d being the thickness of the fractured graphene layers and the thickness of a single graphene layer, respectively. The fracture toughness of graphene, defined as the critical energy release rate, is $G_C = 2\gamma/d$. Finally, τ is the cleavage energy of graphite basal plane, Bl is the cleaved area. When the peeling advances by a virtual distance, dl , it is found that both the relaxation of elastic energy, dU_e , and the cost of cleavage energy, τBdl , are independent on crack angle θ , as detailed in Supplemental Material, Sec. 3. Therefore, according to Eq. (1), the energy favorable crack angle is determined by finding the minimum point of the “fracture force,” $F^* = 2\gamma(\partial s/\partial l)t/d$.

Since the apparently straight steps can consist of nanoscale AC and ZZ segments as sketched in Fig. 4(a), γ should be a weighted average of γ_{AC} and γ_{ZZ} according to the total length of AC and ZZ segments, where γ_{AC} and γ_{ZZ} are edge energy densities along AC and ZZ directions, respectively. An analytical form is given as (detailed in Supplemental Material, Sec. 3):

$$\gamma(\theta) = 2\gamma_{\text{AC}}[\sin\theta + A_\gamma \sin(30^\circ - \theta)], \quad (2)$$

where $A_\gamma = (\gamma_{\text{ZZ}}/\gamma_{\text{AC}}) = (G_{\text{ZZ}}/G_{\text{AC}})$ is the anisotropic factor for edge energy and fracture toughness. G_{ZZ} and G_{AC} are fracture toughness along the ZZ and AC directions. Equation (2) is equivalent to the results derived in Ref. [23] where the differences in density and energy of carbon atoms were considered for ZZ and AC edges, resulting in an anisotropic factor of $A_\gamma = (\sqrt{3}\epsilon_{\text{ZZ}}/2\epsilon_{\text{AC}})$. Here, the

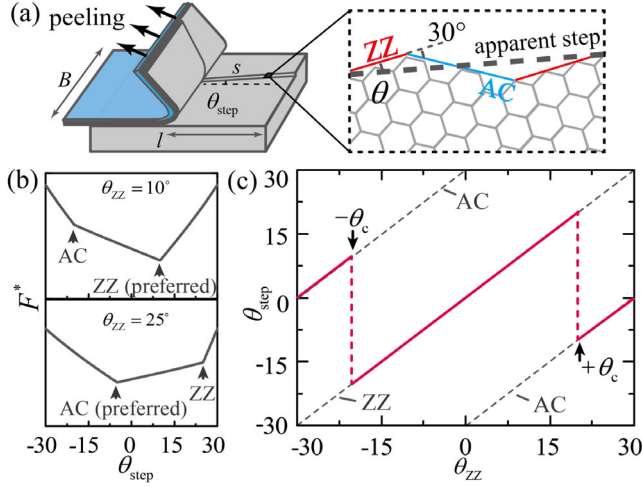


FIG. 4. Theoretical modeling. (a) Schematics showing the model. (b) F^* vs θ_{step} for $\theta_{\text{ZZ}} = 10^\circ$ (upper panel) and $\theta_{\text{ZZ}} = 25^\circ$ (lower panel). The locations of minimum points suggest that the ZZ direction is favorable for $\theta_{\text{ZZ}} = 10^\circ$, while the AC direction is favorable for $\theta_{\text{ZZ}} = 25^\circ$. (c) Theoretical prediction of θ_{step} vs θ_{ZZ} . The step propagates along the ZZ direction if $\theta_{\text{ZZ}} \in (-\theta_c, \theta_c)$, and along the AC direction if otherwise, where θ_c is the critical angle defined by Eq. (3).

energy of a ZZ or AC atom refers to the energy difference of one such atom compared to the bulk state (denoted by ϵ_{ZZ} and ϵ_{AC} , respectively) [23].

For any given lattice orientation (θ_{ZZ}), the preferred step direction (θ_{step}) can be predicted by the above energy arguments. An example is shown in Fig. 4(b), where ZZ and AC directions are found favorable for a small θ_{ZZ} ($\theta_{\text{ZZ}} = 10^\circ$) and large θ_{ZZ} ($\theta_{\text{ZZ}} = 25^\circ$), respectively. In general, a critical angle θ_c is dependent of A_γ as (detailed in Supplemental Material, Sec. 3):

$$\tan(\theta_c) = \frac{2}{A_\gamma} - \sqrt{3}. \quad (3)$$

The step is predicted to follow the ZZ direction, or AC direction, depending on whether the peeling direction is close to the ZZ direction ($|\theta_{\text{ZZ}}| < \theta_c$), or away from the ZZ direction ($|\theta_{\text{ZZ}}| > \theta_c$), as shown in Fig. 4(c). In fact, Fig. 2(d) resembles Fig. 4(c) in a way that many data points are clustered near the ZZ line for small $|\theta_{\text{ZZ}}|$. However, the other data points are scattered as a background noise.

Equation (3) implies that A_γ can be measured if we can evaluate the critical angle θ_c from the experimental data in Fig. 2(d). To do so, we first recall that a step can consist of nanoscale ZZ and AC segments. Therefore, we define the ZZ percentage (in length), p_{ZZ} , for a step with an arbitrary angle $\theta = \theta_{\text{step}} - \theta_{\text{ZZ}}$. An analytical form of p_{ZZ} as a function of θ is explicitly given based on geometry, as detailed in Supplemental Material, Sec. 3. With this definition, all the data points ($\theta_{\text{ZZ}}, \theta_{\text{step}}$) are converted into

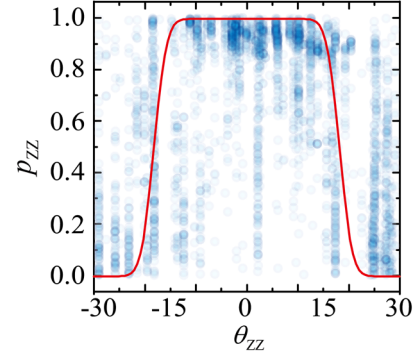


FIG. 5. ZZ percentage (p_{ZZ}) vs ZZ angle (θ_{ZZ}). Data points are extracted from Fig. 2(d). The red line shows the fitting of p_{ZZ} to a smoothed rectangle function, yielding $\theta_c = 18.2^\circ$, corresponding to an anisotropic ratio of $A_\gamma = 0.971$.

($\theta_{\text{ZZ}}, p_{\text{ZZ}}$). Theoretically, the simplified model above predicts the probability of having a ZZ step to be either 1 or 0, depending on whether $|\theta_{\text{ZZ}}|$ is smaller or larger than θ_c . Therefore, $p_{\text{ZZ}}(\theta_{\text{ZZ}})$ should be a rectangle function with discontinuous steps at $\pm\theta_c$. Numerically, a function with smoothed steps, $p_{\text{ZZ}}(\theta_{\text{ZZ}}) = \Phi_{0,\sigma}(\theta_{\text{ZZ}} + \theta_c) - \Phi_{0,\sigma}(\theta_{\text{ZZ}} - \theta_c)$, was used to fit the experimental data and is plotted in Fig. 5, where $\Phi_{0,\sigma}$ is the cumulative distribution function for Gaussian distribution with mean of 0 and standard deviation of σ . An estimation of $\theta_c = 18.2^\circ \pm 0.1$ was calculated, corresponding to $A_\gamma = 0.971 \pm 0.001$. It also implies a ZZ-to-AC probability ratio of $2\theta_c/(30^\circ - \theta_c) = 3.1$, which is in crude agreement with the ZZ-to-AC peak height ratio measured in Fig. 2(c). The smoothing parameter σ was set to 2° here, and its value has negligible effects on the estimated value of θ_c . The physical meaning of σ can be interpreted as an uncertainty of the “effective peeling angle” resulted from random perturbations, as detailed in Supplemental Material, Sec. 4. It is shown in Fig. 5 that the fitting captures the main feature of the data that most steps follow ZZ directions when $|\theta_{\text{ZZ}}|$ is smaller than a threshold value (i.e., θ_c). However, the largely scattered data points in the background, corresponding to the steps containing many nanoscale ZZ and AC segments, seem to disobey this rule. This leads to a relatively large root-mean-square error for the fitting (0.36, which is 36% of the maximum value for p_{ZZ}), despite the apparently small uncertainty for θ_c and A_γ . More details on fitting errors can be found in Supplemental Material, Sec. 4. There are several possible causes of the oscillatory propagation in these cracks, such as the inevitable perturbation of actual peeling angle during the manually controlled exfoliation, and complex local stress field near the crack tip [49]. Intrinsic crack deflection due to asymmetric edge is also found for another 2D material, *h*-BN, recently [11]. The exact physical origin of the winding behavior in graphene steps is currently unclear. The irregularity of step direction due to winding is assumed

as a random noise here, which is a limitation of the present model and harms the validity and accuracy of estimated A_γ .

By geometrical constructions only (i.e., assuming that $\epsilon_{ZZ} = \epsilon_{AC}$), the edge energy density is dependent on the number of broken bonds, which would lead to the conclusion of $A_\gamma = \sqrt{3}/2 \approx 0.866$. However, the estimated value of $A_\gamma = 0.971$ suggests a weaker anisotropy, which may arise from the electronic relaxation at the armchair bonds that lowers the edge energy density by forming triple bonds between the two-coordination carbon atoms [22,23]. A summary on literature results and comparison to the value measured here is given in Supplemental Material, Sec. 5. It is also noted that the extracted fracture toughness is based on the Griffith scenario where dissipative processes such as phonon and electronic excitation or inelastic events are neglected. Therefore, the fracture toughness is simply determined by twice the edge energy, $G_C = 2\gamma/d$. In the real situation, G_C could be larger than this value, and the difference awaits further exploration and discussion.

In conclusion, the anisotropic fracture of graphene is studied by surface steps on cleaved graphite. The morphology and direction of the steps are investigated with respect to the peeling direction and the local lattice orientation on different grains of the polycrystalline HOPG. Part of the steps are well aligned with the local ZZ directions. Meanwhile, the other steps are winding on the nanoscale and show significant irregularity in direction. Combining a mechanics analysis on the fracture process with the statistics of step directions, the anisotropic factor of fracture toughness, or equivalently, edge energy density, is measured as $A_\gamma = G_{ZZ}/G_{AC} = \gamma_{ZZ}/\gamma_{AC} = 0.971$, suggesting that the ZZ direction has a slightly lower fracture toughness. The anisotropy is weaker than the estimation based on geometrical considerations only, implying a relaxation of bonds at the edge. These results provide an experimental benchmark for the widely scattered existing results, offer constraints on future theoretical and simulation models on graphene fracture, and have implications on the fabrication, functioning, and robustness of graphene nanodevices in general.

Q.Z. wishes to acknowledge the financial support by National Natural Science Foundation of China No. 11890671, No. 51961145304, No. 11921002, State Key Laboratory of Tribology Tsinghua University Initiative Scientific Research through Programs No. SKLT2019D02. C. Qu thanks M. Chai from the Center of Nano and Micro Mechanics at Tsinghua University for the help on AFM experiments, and W. Ouyang from Wuhan University for valuable discussions.

*Corresponding author.

qucangyu@seas.upenn.edu

†Corresponding author.

zhengqs@tsinghua.edu.cn

‡Present address: Department of Mechanical Engineering and Applied Mechanics, University of Pennsylvania, Philadelphia, Pennsylvania 19104, USA.

- [1] A. K. Geim and K. S. Novoselov, The rise of graphene, *Nat. Mater.* **6**, 183 (2007).
- [2] K. S. Novoselov, A. K. Geim, S. V. Morozov, D. Jiang, Y. Zhang, S. V. Dubonos, I. V. Grigorieva, and A. A. Firsov, Electric field effect in atomically thin carbon films, *Science* **306**, 666 (2004).
- [3] C. Lee, X. Wei, J. W. Kysar, and J. Hone, Measurement of the elastic properties and intrinsic strength of monolayer graphene, *Science* **321**, 385 (2008).
- [4] K. S. Novoselov, A. K. Geim, S. V. Morozov, D. Jiang, M. I. Katsnelson, I. V. Grigorieva, S. V. Dubonos, and A. A. Firsov, Two-dimensional gas of massless dirac fermions in graphene, *Nature (London)* **438**, 197 (2005).
- [5] P. Zhang, L. Ma, F. Fan, Z. Zeng, C. Peng, P. E. Loya, Z. Liu, Y. Gong, J. Zhang, X. Zhang, P. M. Ajayan, T. Zhu, and J. Lou, Fracture toughness of graphene, *Nat. Commun.* **5**, 3782 (2014).
- [6] Y. Kim, J. Lee, M. S. Yeom, J. W. Shin, H. Kim, Y. Cui, J. W. Kysar, J. Hone, Y. Jung, S. Jeon, and S. M. Han, Strengthening effect of single-atomic-layer graphene in metal-graphene nanolayered composites, *Nat. Commun.* **4**, 2114 (2013).
- [7] S. Stankovich, D. A. Dikin, G. H. B. Dommett, K. M. Kohlhaas, E. J. Zimney, E. A. Stach, R. D. Piner, S. B. T. Nguyen, and R. S. Ruoff, Graphene-based composite materials, *Nature (London)* **442**, 282 (2006).
- [8] M. A. Rafiee, J. Rafiee, I. Srivastava, Z. Wang, H. Song, Z.-Z. Yu, and N. Koratkar, Fracture and fatigue in graphene nanocomposites, *Small* **6**, 179 (2010).
- [9] K. S. Kim, Y. Zhao, H. Jang, S. Y. Lee, J. M. Kim, K. S. Kim, J. H. Ahn, P. Kim, J. Y. Choi, and B. H. Hong, Large-scale pattern growth of graphene films for stretchable transparent electrodes, *Nature (London)* **457**, 706 (2009).
- [10] J. Annett and G. L. W. Cross, Self-assembly of graphene ribbons by spontaneous self-tearing and peeling from a substrate, *Nature (London)* **535**, 271 (2016).
- [11] Y. Yang, Z. Song, G. Lu, Q. Zhang, B. Zhang, B. Ni, C. Wang, X. Li, L. Gu, X. Xie, H. Gao, and J. Lou, Intrinsic toughening and stable crack propagation in hexagonal boron nitride, *Nature (London)* **594**, 57 (2021).
- [12] X. Zhang, J. Xin, and F. Ding, The edges of graphene, *Nanoscale* **5**, 2556 (2013).
- [13] T. Kawai, Y. Miyamoto, O. Sugino, and Y. Koga, Graphitic ribbons without hydrogen-termination: Electronic structures and stabilities, *Phys. Rev. B* **62**, R16349 (2000).
- [14] L. Sun, P. Wei, J. Wei, S. Sanvito, and S. Hou, From zigzag to armchair: The energetic stability, electronic and magnetic properties of chiral graphene nanoribbons with hydrogen-terminated edges, *J. Phys. Condens. Matter* **23**, 425301 (2011).
- [15] Z. Chen, Y. M. Lin, M. J. Rooks, and P. Avouris, Graphene nano-ribbon electronics, *Phys. E Low-Dimensional Syst. Nanostructures* **40**, 228 (2007).
- [16] X. Li, X. Wang, L. Zhang, S. Lee, and H. Dai, Chemically derived, ultrasmooth graphene nanoribbon semiconductors, *Science* **319**, 1229 (2008).
- [17] C. Daniels, A. Horning, A. Phillips, D. V. P. Massote, L. Liang, Z. Bullard, B. G. Sumpter, and V. Meunier, Elastic, plastic, and fracture mechanisms in graphene materials, *J. Phys. Condens. Matter* **27**, 373002 (2015).

- [18] H. Yin, H. J. Qi, F. Fan, T. Zhu, B. Wang, and Y. Wei, Griffith criterion for brittle fracture in graphene, *Nano Lett.* **15**, 1918 (2015).
- [19] M. A. N. Dewapriya and S. A. Meguid, Tailoring fracture strength of graphene, *Comput. Mater. Sci.* **141**, 114 (2018).
- [20] B. Zhang, L. Mei, and H. Xiao, Nanofracture in graphene under complex mechanical stresses, *Appl. Phys. Lett.* **101**, 121915 (2012).
- [21] M. Q. Le and R. C. Batra, Mode-I stress intensity factor in single layer graphene sheets, *Comput. Mater. Sci.* **118**, 251 (2016).
- [22] C. K. Gan and D. J. Srolovitz, First-principles study of graphene edge properties and flake shapes, *Phys. Rev. B* **81**, 125445 (2010).
- [23] Y. Liu, A. Dobrinsky, and B. I. Yakobson, Graphene Edge from Armchair to Zigzag: The Origins of Nanotube Chirality?, *Phys. Rev. Lett.* **105**, 235502 (2010).
- [24] P. Koskinen, S. Malola, and H. Häkkinen, Self-Passivating Edge Reconstructions of Graphene, *Phys. Rev. Lett.* **101**, 115502 (2008).
- [25] J. Gao, J. Yip, J. Zhao, B. I. Yakobson, and F. Ding, Graphene nucleation on transition metal surface: Structure transformation and role of the metal step edge, *J. Am. Chem. Soc.* **133**, 5009 (2011).
- [26] K. Kim, V. I. Artyukhov, W. Regan, Y. Liu, M. F. Crommie, B. I. Yakobson, and A. Zettl, Ripping graphene: Preferred directions, *Nano Lett.* **12**, 293 (2012).
- [27] F. Liu, P. Ming, and J. Li, Ab initio calculation of ideal strength and phonon instability of graphene under tension, *Phys. Rev. B* **76**, 064120 (2007).
- [28] M. Xu, J. T. Paci, J. Oswald, and T. Belytschko, A constitutive equation for graphene based on density functional theory, *Int. J. Solids Struct.* **49**, 2582 (2012).
- [29] M. Z. Hossain, T. Ahmed, B. Silverman, M. S. Khawaja, J. Calderon, A. Rutten, and S. Tse, Anisotropic toughness and strength in graphene and its atomistic origin, *J. Mech. Phys. Solids* **110**, 118 (2018).
- [30] K. Kim, S. Coh, C. Kisielowski, M. F. Crommie, S. G. Louie, M. L. Cohen, and A. Zettl, Atomically perfect torn graphene edges and their reversible reconstruction, *Nat. Commun.* **4**, 2723 (2013).
- [31] M. V. Rastei, A. Craciun, M. El Abbassi, M. Diebold, P. Cotte, O. Ersen, H. Bulou, and J. L. Gallani, Anisotropic failure of sp^2 -hybrid bonds in graphene sheets, *J. Phys. Chem. C* **123**, 28469 (2019).
- [32] S. Neubeck, Y. M. You, Z. H. Ni, P. Blake, Z. X. Shen, A. K. Geim, and K. S. Novoselov, Direct determination of the crystallographic orientation of graphene edges by atomic resolution imaging, *Appl. Phys. Lett.* **97**, 053110 (2010).
- [33] X. Jia, M. Hofmann, V. Meunier, B. G. Sumpter, J. Campos-Delgado, J. M. Romo-Herrera, H. Son, Y.-P. Hsieh, A. Reina, J. Kong, M. Terrones, and M. S. Dresselhaus, Controlled formation of sharp zigzag and armchair edges in graphitic nanoribbons, *Science* **323**, 1701 (2009).
- [34] M. Fujihara, R. Inoue, R. Kurita, T. Taniuchi, Y. Motoyui, S. Shin, F. Komori, Y. Maniwa, H. Shinohara, and Y. Miyata, Selective formation of zigzag edges in graphene cracks, *ACS Nano* **9**, 9027 (2015).
- [35] L. Shi, L. Yang, J. Deng, L. Tong, Q. Wu, L. Zhang, L. Zhang, L. Yin, and Z. Qin, Constructing graphene nanostructures with zigzag edge terminations by controllable STM tearing and folding, *Carbon* **165**, 169 (2020).
- [36] C. O. Girit, J. C. Meyer, R. Erni, M. D. Rossell, C. Kisielowski, L. Yang, C.-H. Park, M. F. Crommie, M. L. Cohen, S. G. Louie, and A. Zettl, Graphene at the edge: Stability and dynamics, *Science* **323**, 1705 (2009).
- [37] Y. Kolombus, A. Zalic, N. Fardian-Melamed, Z. Barkay, D. Rotem, D. Porath, and H. Steinberg, Crystallographic orientation errors in mechanical exfoliation, *J. Phys. Condens. Matter* **30**, 475704 (2018).
- [38] Y. Kobayashi, K. I. Fukui, T. Enoki, and K. Kusakabe, Edge state on hydrogen-terminated graphite edges investigated by scanning tunneling microscopy, *Phys. Rev. B* **73**, 125415 (2006).
- [39] E. Hamm, P. Reis, M. LeBlanc, B. Roman, and E. Cerda, Tearing as a test for mechanical characterization of thin adhesive films, *Nat. Mater.* **7**, 386 (2008).
- [40] E. Gao, S. Z. Lin, Z. Qin, M. J. Buehler, X. Q. Feng, and Z. Xu, Mechanical exfoliation of two-dimensional materials, *J. Mech. Phys. Solids* **115**, 248 (2018).
- [41] H. Lee, H. B. R. Lee, S. Kwon, M. Salmeron, and J. Y. Park, Internal and external atomic steps in graphite exhibit dramatically different physical and chemical properties, *ACS Nano* **9**, 3814 (2015).
- [42] H. Hölscher, D. Ebeling, and U. D. Schwarz, Friction at Atomic-Scale Surface Steps: Experiment and Theory, *Phys. Rev. Lett.* **101**, 246105 (2008).
- [43] Z. Chen, A. Khajeh, A. Martini, and S. H. Kim, Chemical and physical origins of friction on surfaces with atomic steps, *Sci. Adv.* **5**, eaaw0513 (2019).
- [44] Z. Ye and A. Martini, Atomic friction at exposed and buried graphite step edges: Experiments and simulations, *Appl. Phys. Lett.* **106**, 231603 (2015).
- [45] See Supplemental Material at <http://link.aps.org/supplemental/10.1103/PhysRevLett.129.026101>, which includes experimental methods, extended data on step morphology, derivations of theoretical model, data fitting and errors, comparison with literature results, and Refs. [46–47].
- [46] S. Y. Park, H. C. Floresca, Y. J. Suh, and M. J. Kim, Electron microscopy analyses of natural and highly oriented pyrolytic graphites and the mechanically exfoliated graphenes produced from them, *Carbon* **48**, 797 (2010).
- [47] C. Y. Hui, A. T. Zehnder, and Y. K. Potdar, Williams meets von Karman: Mode coupling and nonlinearity in the fracture of thin plates, *Int. J. Fract.* **93**, 409 (1998).
- [48] D. L. C. Ky, B.-C. Tran Khac, C. T. Le, Y. S. Kim, and K.-H. Chung, Friction characteristics of mechanically exfoliated and CVD-grown single-layer MoS_2 , *Friction* **6**, 395 (2018).
- [49] X. Huang, H. Yang, A. C. T. van Duin, K. J. Hsia, and S. Zhang, Chemomechanics control of tearing paths in graphene, *Phys. Rev. B* **85**, 195453 (2012).

Anisotropic Fracture of Graphene Revealed by Surface Steps on Graphite

*Cangyu Qu**, *Diwei Shi*, *Li Chen*, *Zhanghui Wu*, *Jin Wang*, *Songlin Shi*, *Enlai Gao*, *Zhiping Xu*, *Quanshui Zheng**

1. Experimental methods

Mechanical exfoliation

The peeling of the graphite sample was controlled manually, with a peeling speed as low as possible, roughly on the order of 0.1 to 1 mm/s. The purpose of using a small peeling speed is to have a peeling speed that is much lower than the speed of elastic waves in graphite so that the mechanical loading can be treated as quasi-static.

The peeling direction was usually parallel to one edge of the rectangular-shaped graphite sample. Then the sample was transferred to AFM with the same edge aligned with the coordinate system in AFM defined by the scanning direction. Since the peeling process is conducted manually, we cannot precisely measure the peeling speed, peeling angle, or peeling force. This is one possible origin of uncertainty in our experiments.

Step angle measurement

Steps are shown in the AFM friction images as bright (high-friction) lines. A typical result is shown in Fig. S1. Also shown in Fig. S1(a) are grain boundaries (GBs). Both GBs and steps appear as bright lines in the friction image, but they can be distinguished in the height image, where steps show abrupt change in height while GBs do not. Each step was manually labeled [red lines in Fig. S1(b)], then a customized computer program was used to extract the step angle from the labeled image. The uncertainty of the step angle (θ_{step}) can be estimated as the standard error of repeated measurements on a same step, which is typically on the order of 1°.

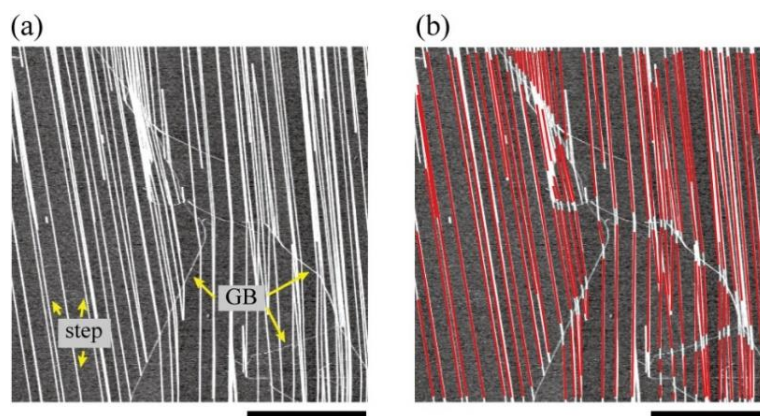


Figure S1. Measurement of step angle by AFM. (a) AFM friction image. Steps are shown as bright (high frictional) lines. Also shown are grain boundaries (GBs). (b) Steps are labeled in red color, then a customized code is used to extract their angles. Scale bars, 10 μm .

Lattice angle measurement

To determine the lattice orientation using AFM, a small area (usually 5 nm \times 5 nm) at a given position was scanned by AFM in lateral force mode, using a compliant cantilever (VIT-P-C, NT-MDT & TipsNano, spring constant 0.2 N/m). A typical lateral force image is shown in Fig. S2(a). The lattice orientation can be extracted from the fast Fourier transformation (FFT) of the raw image as shown in Fig. S2(b), or from the filtered lateral force image as shown in Fig. S2(c). It is also measured in Fig. S2(c) that the distance between adjacent hollow sites of the graphene lattice is around 2.59 \AA , corresponding to a carbon-carbon bond length of 1.49 \AA , which is consistent with the theoretical bond length in graphene lattice $a = 1.42 \text{\AA}$. The uncertainty of the lattice angle (θ_{ZZ}) is estimated as the standard error of angle measurements on a series of images of repeated scanning at the same position. And the standard error is typically below 3 $^\circ$.

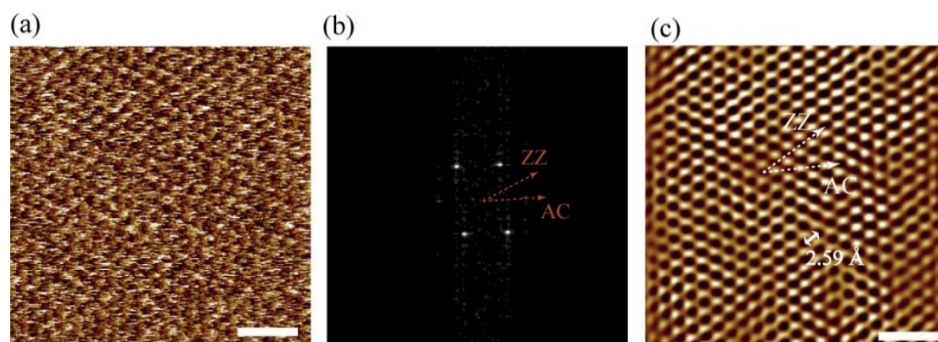


Figure S2. Determination of lattice orientation by AFM. (a) Raw image (lateral force) of a 5 nm \times 5 nm area on graphite surface. (b) Fast Fourier transform (FFT) of the raw image. ZZ and AC directions are labeled by the red arrows. (c) Filtered lateral force image. ZZ and AC directions are labeled by the white arrows. The distance between adjacent hollow sites is measured to be 2.59 \AA , corresponding to carbon-carbon bond length of 1.49 \AA . Scale bars in (a) and (c) are 1 nm.

2. Extended data on step morphology

Step height

Height of the steps are extracted from AFM height images. The histogram for over 1500 steps on 10 different regions is shown in Fig. S3. The majority of the steps have height less than 1 nm, corresponding to the thickness of 1~3 layers of graphene. The highest step found is around 4.6 nm.

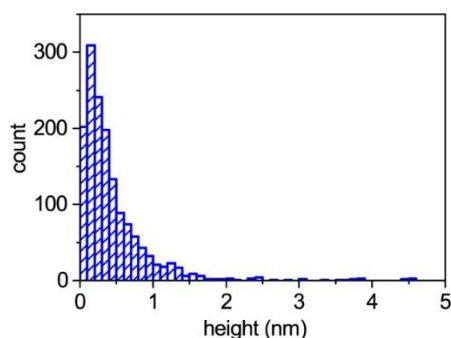


Figure S3. Histogram for step height. Most of the steps have height less than 1 nm, corresponding to 1~3 layers of graphene.

Lateral density of steps

The lateral density of steps is defined as the total length of all steps in a grain divided by the area of this grain. The density defined in this way, hereafter denoted as λ , has a unit of μm^{-1} . And $1/\lambda$ represents the effective mean distance between two adjacent steps.

Density of steps was calculated for data from 2779 steps found in 97 different grains in total. Figure S4 shows that step density is scattered within the range of 0.02 to $1.7 \mu\text{m}^{-1}$, with a mean value of $0.9 \mu\text{m}^{-1}$, and that no significant dependence on θ_{ZZ} is found.

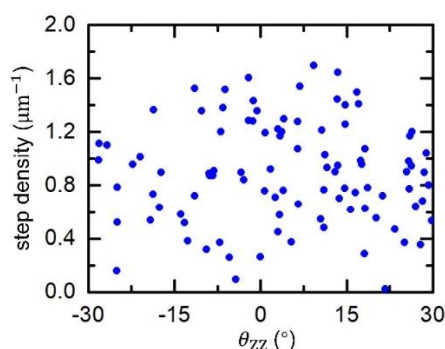


Figure S4. Step density vs. θ_{ZZ} for data corresponding to 2779 steps in 97 different grains. No significant trend is found.

Steps on h-BN, MoS₂, and flake graphite

Although we did not find an obvious dependence of step density on grain orientation, we did observe that step density can be very different for cleaved surfaces of HOPG and flake graphite, as well as h-BN and MoS₂. Mechanical exfoliation was conducted for h-BN, MoS₂, and natural

flake graphite. Optical microscope images and AFM height and friction images of the cleaved surfaces are shown in Fig. S5. As a comparison, results for HOPG are also included. High steps that are visible under optical microscope are found for all these layered materials. However, when scanned under AFM, a difference is observed on h-BN, MoS₂, and flake graphite. For HOPG, apart from the high steps visible under optical microscope, there are also many atomic steps that can be observed by AFM but invisible under optical microscope [see Figs. S5(k)(l)]. However, for the other three layered materials, these atomic steps are seldomly found. Overall, the steps are much fewer in number, and thus provide inadequate data for determining fracture anisotropy. A possible reason is that these materials tend to have much larger grain size than HOPG, with the latter being well-known as polycrystalline material containing micrometer to nanometer sized grains [1]. The grain boundaries in HOPG might act as nucleation sites for cracks, and leads to a denser distribution of surface steps which is not seen on the three crystals with larger grain size.

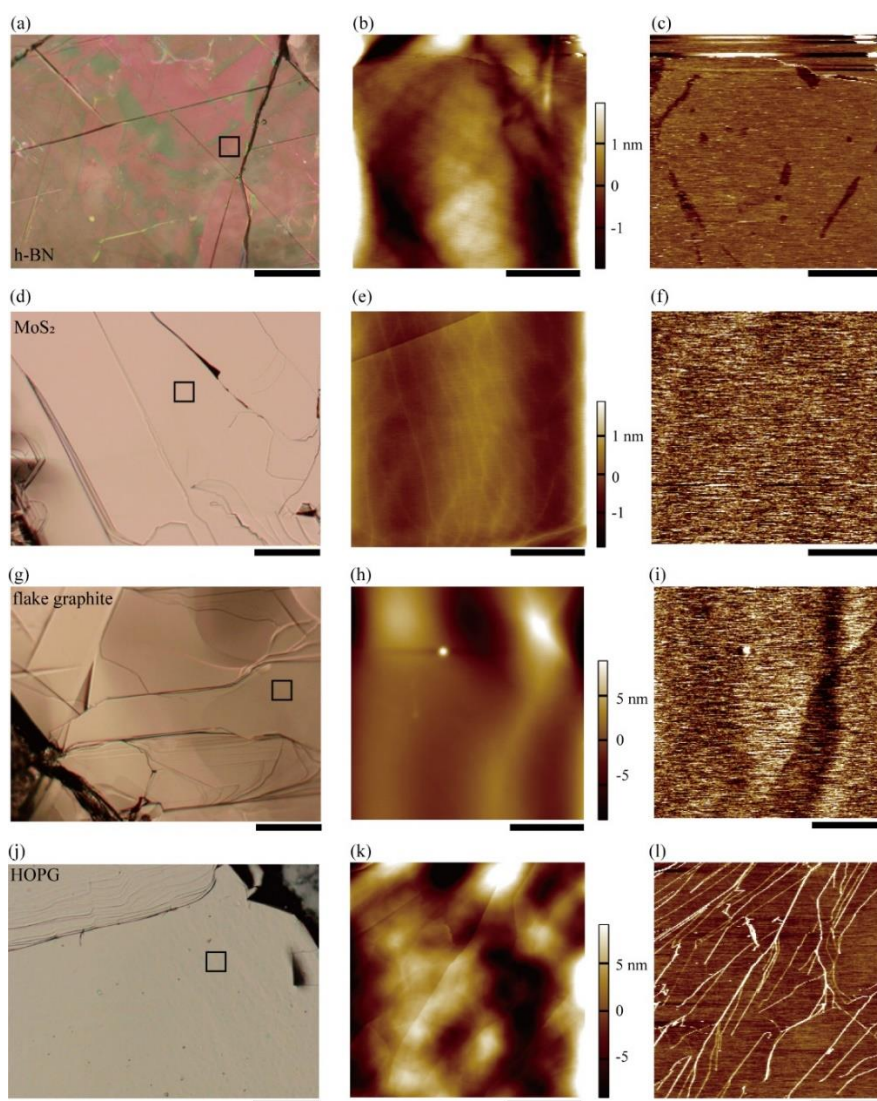


Figure S5. Comparison of cleaved surfaces of h-BN, MoS₂, flake graphite, and HOPG. Subfigures (a), (d), (g), and (j) are optical microscope images, and the black boxes indicate the area for AFM

scans. Subfigures (b), (e), (h), and (k) are AFM height images. And subfigures (c), (f), (i), and (l) are AFM friction images. All the scale bars in optical images are 100 μm , while those in AFM images are 10 μm .

“Branched” steps

“Branched” steps were occasionally observed in the friction image, such as the one indicated by the red arrow in Fig. S6(b). However, on the height image, Fig. S6(a), it is seen that these are not branched steps, but instead, steps of different height stacked together. To show this, a section profile is drawn at the position indicated by the red line, and shown in Fig. S6(c). Five terraces (labeled A to E) are divided by 4 steps. The step between terraces A and B is 1.1 nm high, equivalent to around 3 layers of graphene. Meanwhile, that between B and C is 0.4 nm (\sim 1 layer); and C and D, 0.7 nm (\sim 2 layers); and finally D and E, 1.8 nm (\sim 5 layers). The steps have different height, although they all just appear as bright lines in the friction image. The highest step (the step between D and E) is made of around 5 layers of graphene, and the crack paths in these 5 layers happen to coincide to form one single step. However, on the other side of the terrace, the crack paths of the 5 layers do not coincide. And more than one steps are formed. In the friction image, it appears that the steps are branched.

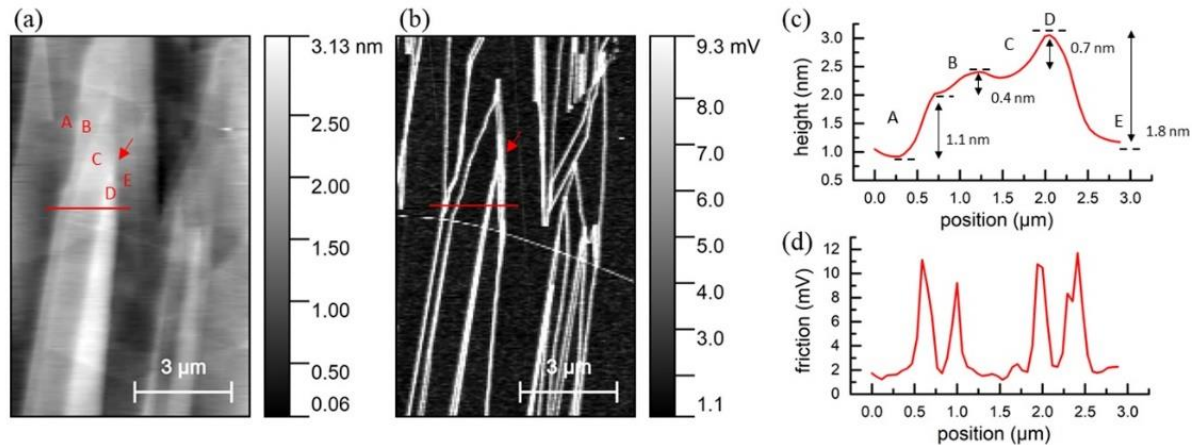


Figure S6. (a) AFM height image and (b) the corresponding friction image. Red arrow indicates an apparent “branched step”. (c)(d) Profiles for the height and friction at the location indicated by the red lines in (a) and (b).

Segment length and connecting corners

It is discussed in the main text that some steps that appear to be straight on the microscale are actually made of ZZ and AC segments connected by corners. The energy of an edge with an arbitrary angle is given by Eq. (2). This equation considers γ as a weighted function of the energies of AC and ZZ segments, γ_{AC} and γ_{ZZ} . In principle, a correction term should be added to account for the energy of those corners connecting ZZ and AC segments. This correction was discussed in Ref. [2], termed as “AZ-mix energy correction”. It was estimated that this correction term is in the range of 10 meV/Å, 100 times smaller than γ_{AC} and γ_{ZZ} which are both around 1 eV/Å, and is neglected in this work.

Systematic investigation of segment length and the density of connecting corners, as well as their dependence on other peeling parameters is difficult. To have a clear image of the corner

and the segments it connects, the resolution needs to be on the lattice scale, such as Fig. 3(d). However, to obtain any statistical quantities, a large number of segments need to be imaged, which means that the image size has to be at least hundreds of nanometers. This mismatch of scales makes the imaging challenging.

Despite the technical difficulties, a lower-resolution image of two steps containing some segments and corners is shown in Fig. S7(a). In the histogram, Fig. S7(b), it is found that most of the segments are along two different ZZ directions separated by 60° . The average segment length is 6.9 nm, corresponding to a corner density of 0.14 nm^{-1} . Considering that the lattice constant of graphene in ZZ direction is 2.46 \AA , a corner is expected every 28 unit cells on average. Segments that appear to be neither ZZ nor AC are found, and most of them have shorter length, as shown in Fig. S7(c). The angle measurement for a short segment might have larger uncertainty, and we do not know whether these segments are made of even shorter ZZ and AC segments due to the limitation on resolution. In fact, when seen on the lattice scale, all edges can be considered as connection of very short ZZ and AC segments with length of only several lattice constants. Due to the limited resolution and small size of dataset, the results shown in Fig. S7 should be only considered as an example, further study is needed on the nanoscale topography and behavior of step segments.

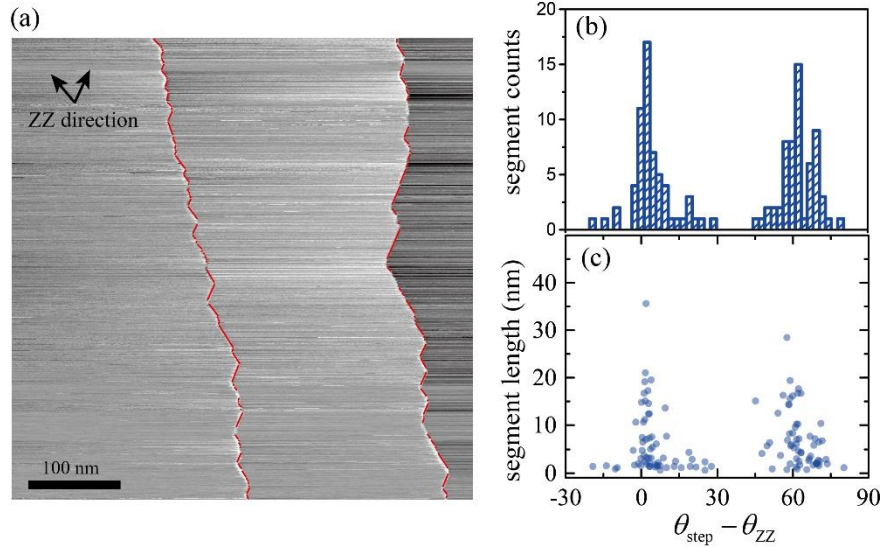


Figure. S7. (a) AFM image of two steps that contain segments. (b) Histogram of segment angle. (c) Segment length vs. segment angle.

3. Derivations of theoretical model

Energy favorable crack direction

As described in the main text, the total energy associated with the fracture process is:

$$U = U_B + U_T + 2\gamma ts/d + \tau Bl. \quad (\text{S1})$$

Here $U_B + U_T$ is the total elastic strain energy, where U_B and U_T are the bending and tensile energies of the tape and the graphite film adhered to the tape. Since the fractured fragment (whose thickness is only 1~3 layers of graphene according to step height measurements) is much thinner than the tape itself. It is reasonable to assume that the elastic energy is mainly

contributed from the tape and the graphite film adhered to the tape. Therefore, the tensile energy is:

$$U_T = \frac{1}{2}EA\Delta^2/l, \quad (\text{S2})$$

where EA is the tensile stiffness, and Δ is the tensile deformation. Meanwhile, the bending energy was given in Ref. [3] as:

$$U_B = \sqrt{2FEI} \left(\sqrt{2} - \frac{\sin \alpha}{\sqrt{1-\cos \alpha}} \right), \quad (\text{S3})$$

where EI is the bending stiffness. It is noted that U_B is independent on l , θ_{step} , or s . From geometric relations as shown in Fig. S8, we have:

$$\delta\Delta = \delta x - (1 + \cos \alpha)\delta l. \quad (\text{S4})$$

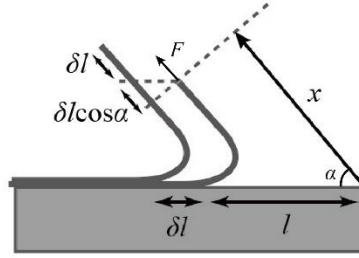


Figure S8. Schematic of the peeling process (side view).

According to Griffith theory, equilibrium propagation of the crack requires $\partial U/\partial s = 0$. Therefore, taking the derivative of Eq. (S1) with respect to s , and combing it with the geometric relation $\delta l = \cos(\theta_{\text{step}}) \delta s$ yields:

$$\frac{\partial U_T}{\partial s} + 2\gamma t/d + \tau B \cos(\theta_{\text{step}}) = 0. \quad (\text{S5})$$

Meanwhile, taking the s -derivative of Eq. (S2) at a fixed x (i.e. $\delta x = 0$) and combining with Eq. (S4) yields:

$$\frac{\partial U_T}{\partial s} = \frac{\partial U_T}{\partial l} \cos(\theta_{\text{step}}) = -\frac{EA}{2} \cdot \left[\frac{2\Delta}{l} (1 + \cos \alpha) + \left(\frac{\Delta}{l} \right)^2 \right] \cos(\theta_{\text{step}}). \quad (\text{S6})$$

Considering that $\frac{EA\Delta}{l} = F$, where F is the peeling force, Eq. (S6) is equivalent to

$$\frac{\partial U_T}{\partial s} = -\cos(\theta_{\text{step}}) \left[F(1 + \cos \alpha) + \frac{F^2}{2EA} \right]. \quad (\text{S7})$$

Substituting Eq. (S7) into Eq. (S5) yields:

$$-\cos(\theta_{\text{step}}) \left[F(1 + \cos \alpha) + \frac{F^2}{2EA} \right] + 2\gamma t/d + \tau B \cos(\theta_{\text{step}}) = 0. \quad (\text{S8})$$

For $\alpha < \pi/2$, $1 + \cos \alpha$ is greater than 1, while $\frac{F}{EA}$ is the tensile strain and should be much smaller than 1. Thus, Eq. (S8) can be further simplified as:

$$-\cos(\theta_{\text{step}}) F(1 + \cos \alpha) + 2\gamma t/d + \tau B \cos(\theta_{\text{step}}) = 0. \quad (\text{S9})$$

Therefore:

$$F = \left[\frac{2\gamma t}{\cos(\theta_{\text{step}}) \cdot d} + \tau B \right] / (1 + \cos \alpha). \quad (\text{S10})$$

In the experiment condition, peeling was conducted in a manner that $\alpha \approx 0$. the propagation angle of the crack (θ_{step}) should be the point where F finds its minimum [4]. Here the anisotropic edge energy, γ , is a function of $\theta = \theta_{\text{step}} - \theta_{\text{ZZ}}$. It can be seen from Eq. (S10) that F only depends on θ through $F^* = \frac{2\gamma t}{\cos(\theta_{\text{step}}) \cdot d}$. Since F^* has a dimension of force, we might name it as the ‘‘fracture force’’ [4]. The determination of energy favorable crack angle comes down to finding the minimum point of F^* .

Derivations of Eq. (2) and calculation of p_{ZZ}

We remind that some of the steps consist of nanoscale ZZ and AC step segments, so that their apparent directions are neither ZZ nor AC. A step with an arbitrary angle θ is sketched in Fig. S9. For an apparent step with length L_0 , the actual total length of ZZ segments is $L_1 = L_0 \sin(30^\circ - \theta) / \sin 150^\circ$, and the actual total length of AC segments is $L_2 = L_0 \sin \theta / \sin 150^\circ$. Therefore, the apparent edge energy density is a weighted average of γ_{AC} and γ_{ZZ} as:

$$\gamma(\theta) = \frac{L_2}{L_0} \cdot \gamma_{\text{AC}} + \frac{L_1}{L_0} \cdot \gamma_{\text{ZZ}} = 2 \sin \theta \cdot \gamma_{\text{AC}} + 2 \sin(30^\circ - \theta) \cdot \gamma_{\text{ZZ}}. \quad (\text{S11})$$

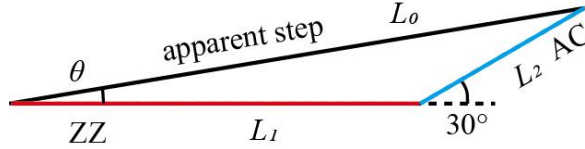


Figure S9. Sketch of the apparent step and its consisting ZZ and AC segments.

Similar geometric considerations were also exploited in the extraction of θ_C from experimental data. We assume that a step with an arbitrary angle θ is made of a portion of p_{ZZ} of zigzag step and a portion of $1 - p_{\text{ZZ}}$ of armchair step, and the zigzag percentage p_{ZZ} as a function of θ is defined as:

$$p_{\text{ZZ}}(\theta) = \frac{L_1}{L_1 + L_2} = \frac{\cos \theta - \sqrt{3} \sin \theta}{\cos \theta + (2 - \sqrt{3}) \sin \theta}. \quad (\text{S12})$$

With this definition, all the data points $(\theta_{\text{ZZ}}, \theta_{\text{step}})$ are converted into $(\theta_{\text{ZZ}}, p_{\text{ZZ}})$. And p_{ZZ} was then fitted to a step-like function to extract the value of θ_C , as detailed later in this supplementary file.

Derivations of Eq. (3)

Equation (3) in the main text gives an analytical relation between θ_C and A_γ . The critical angle, θ_C , is the value of θ_{ZZ} where the minimum point of function $F^*(\theta) \sim \gamma(\theta)/\cos(\theta + \theta_{ZZ})$ changes from $\theta = 0$ to $\theta = -30^\circ$, where $\theta = \theta_{\text{step}} - \theta_{ZZ}$ is the cracking angle.

Calculations yield:

$$\frac{\gamma(0)}{\cos(0+\theta_{ZZ})} = \frac{2\gamma_{AC} \cdot A_\gamma \sin 30^\circ}{\cos \theta_{ZZ}}. \quad (\text{S13})$$

Meanwhile,

$$\frac{\gamma(30^\circ)}{\cos(\theta_{ZZ}-30^\circ)} = \frac{2\gamma_{AC} \cdot \sin 30^\circ}{\cos(\theta_{ZZ}-30^\circ)}. \quad (\text{S14})$$

Therefore,

$$A_\gamma \cdot \cos(\theta_C - 30^\circ) = \cos \theta_C. \quad (\text{S15})$$

Thus we derived Eq. (3):

$$\tan \theta_C = \frac{2}{A_\gamma} - \sqrt{3}. \quad (\text{S16})$$

4. Data fitting and errors

Data fitting in Fig. 5

The theoretical model predicts that the step either follows ZZ or AC direction depending on whether $|\theta_{ZZ}|$ is smaller or larger than θ_C . Therefore, the ZZ percentage function should be:

$$p_{ZZ}(\theta_{ZZ}) = \begin{cases} 1, & |\theta_{ZZ}| < \theta_C \\ 0, & |\theta_{ZZ}| > \theta_C \end{cases}. \quad (\text{S17})$$

To extract the value of θ_C , the datapoints in Fig.5 should be fitted to Eq. (S17). However, the discontinuity at $\pm\theta_C$ makes such a fitting numerically difficult. Instead of Eq. (S17), the following function is used:

$$p_{ZZ}(\theta_{ZZ}) = \Phi_{0,\sigma}(\theta_{ZZ} + \theta_C) - \Phi_{0,\sigma}(\theta_{ZZ} - \theta_C), \quad (\text{S18})$$

where $\Phi_{0,\sigma}$ is the cumulative distribution function for Gaussian distribution with mean of 0 and standard deviation of σ . This function has smoothed steps at $\pm\theta_C$, and it approaches the function given in Eq. (S17) when σ approaches 0. A reasonably small value of 2° is chosen for σ . A least square fit yields the curve in Fig. 5 and θ_C value reported in the main text. Physically, the smoothing parameter σ can be interpreted as an uncertainty of the actual peeling angle. In this scenario, the actual peeling angle, δ , is not perfectly known, but instead, assumed to follow a Gaussian distribution with mean of 0 and standard deviation of σ . The ZZ percentage function is thus given by $p_{ZZ}(\theta_{ZZ}) = p(-\theta_C < \theta_{ZZ} - \delta < \theta_C) = p(\theta_{ZZ} - \theta_C < \delta < \theta_{ZZ} +$

θ_C), yielding the same result as Eq. (S18). The fitted value of θ_C show negligible dependence on σ as shown in Fig. S10, which validates the fitting and choice of σ .

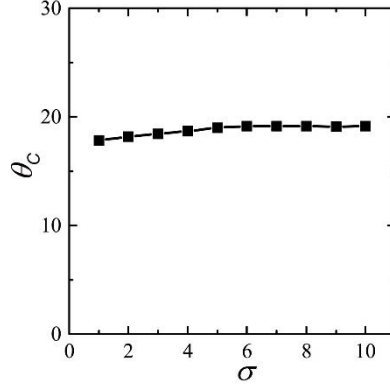


Figure S10. The fitted value of θ_C has negligible dependence on the value of σ .

Fitting errors in Fig. 5

The datapoints in Fig. 5 were fitted to Eq. (S18) with a least square fit algorithm using MATLAB. The root-mean-square error of the fitting is given as $\text{RMSE} = \sqrt{S/(N-1)}$, where S is the sum of squared errors, and N is the number of datapoints. The standard deviation of estimated θ_C is $\sigma_{\theta_C} = \text{RMSE}/\sqrt{\mathbf{J}^T \mathbf{J}}$, where the Jacobian, \mathbf{J} , is an N -by-1 matrix. The uncertainty of A_γ is calculated from the uncertainty of θ_C by taking the derivative of Eq. (3), which yields

$$\sigma_{A_\gamma} = \frac{A_\gamma^2}{2(\cos \theta_C)^2} \sigma_{\theta_C}.$$

The apparent uncertainty of θ_C and A_γ is very small. However, we do not intend to claim that an accurate measurement has been achieved. This is because that the root-mean-square error of the fitting is relatively large ($\text{RMSE} = 0.36$, that is, 36% of the maximum value of p_{ZZ}). This relatively large root-mean-square error is resulted from the fact that a large portion of data is scattered irregularly as a background noise to the datapoints clustered near $p_{ZZ} = 1$ (ZZ direction). And the scattered datapoints correspond to the steps containing nanoscale ZZ and AC segments. Therefore, the major limitation of the current work is that the winding behavior of those steps with irregular directions is not fully included in the present model, and that harms the validity and accuracy on the measurement of A_γ .

Histogram in Fig. 2(c)

Histogram of $\theta_{\text{step}} - \theta_{ZZ}$ is produced by firstly counting the number of datapoints lying in each bin of $\theta_{\text{step}} - \theta_{ZZ}$ ranging from -30° to 30° , and then calculating the data frequency normalized by data density with respect to θ_{ZZ} . The purpose of the normalization is to account

for the effect of a non-uniform distribution of data-points in θ_{ZZ} . However, the two histograms before and after normalization, as shown in Fig. S11, show only minute difference.

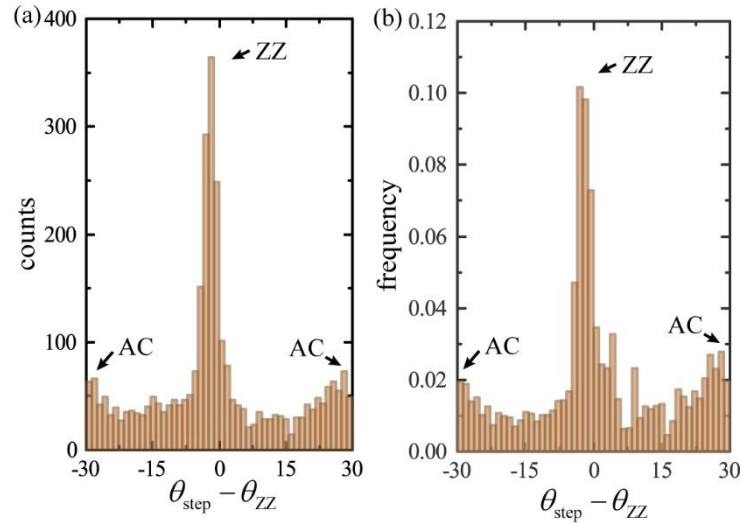


Figure S11. Histograms before (a) and after (b) normalization.

5. Comparison with literature results

Literature results on A_γ

Some theoretical results on edge energy in literature are summarized in Table S1. Here γ_{ZZ} and γ_{AC} (in the unit of eV/Å) are the edge energy densities along ZZ and AC directions. For those literatures where fracture toughness G_C (in the unit of J/m²) is given, edge energy is deduced as $\gamma = G_C d/2$, where $d = 0.34$ nm is the thickness of a single graphene layer.

Table S1. Summary of theoretical results on edge energy in literature.

Method	γ_{ZZ} (eV/Å)	γ_{AC} (eV/Å)	A_γ	Ref.
DFT	1.27	0.95	1.33	Ref. [5]
DFT	1.391	1.202	1.16	Ref. [6]
DFT	1.543	1.202	1.28	Ref. [6]
DFT (GGA)	1.17	1.01	1.16	Ref. [2]
DFT (LDA)	1.38	1.11	1.24	Ref. [2]
DFT	1.31	0.98	1.34	Ref. [7]
DFT	1.346	1.009	1.33	Ref. [8]

DFT	0.96	0.98	0.98	Ref. [7]
DFT	1.147	1.202	0.95	Ref. [6]
MD (ReaxFF)	1.08	1.03	1.05	Ref. [9]
MD (AIREBO)	1.17	1.69	0.69	Ref. [5]
MD (AIREBO)	1.17	1.24	0.94	Ref. [5]
MD (REBO)	1.25	1.33	0.94	Ref. [10]
MD (AIREBO)	1.08	1.16	0.93	Ref. [2]
MD (REBO)	1.25	1.31	0.95	Ref. [2]

Strength-based fracture criterion and literature results on A_σ

Other than the energy-based criterion discussed in the main text, the direction of step can be determined by strength-based fracture criterion as well. The stress field close to the crack-tip during the mechanical exfoliation of graphene has not been understood completely. However, here we might assume that the mode III far-field loading in the peeling process leads to a stress distribution near the crack tip which is described by the classical mode I asymptotic field [11,12]. Consider that a pre-crack exists along the peeling direction (the horizontal direction in Fig. S12), and the circumferential stress is:

$$\sigma_{\theta\theta} = \frac{K}{\sqrt{2\pi r}} \cos^3 \frac{\theta}{2} \quad (\text{S19})$$

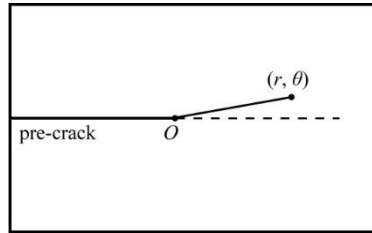


Figure S12. Sketch for strength-based fracture criterion.

where r and θ are the polar coordinates, K is the mode I stress intensity factor. We might assume that the closest ZZ direction is at an angle of $\theta = \theta_{ZZ}$, then the closest AC direction is at $\theta = 30^\circ - \theta_{ZZ}$. At any given angle, the ratio between the local circumferential stress and the local fracture strength of graphene is $\sigma_{\theta\theta}/\sigma_s$. When the peeling direction is close to ZZ direction, i.e., $|\theta_{ZZ}| < \theta_C$. This ratio is larger for ZZ direction than AC direction, i.e., $\sigma_{\theta\theta}(\theta_{ZZ})/\sigma_{ZZ} > \sigma_{\theta\theta}(30^\circ - \theta_{ZZ})/\sigma_{AC}$, where σ_{ZZ} and σ_{AC} are the strength of graphene under tensile loading perpendicular to ZZ and AC directions, respectively. Similarly, for $|\theta_{ZZ}| > \theta_C$,

we have $\sigma_{\theta\theta}(\theta_{ZZ})/\sigma_{ZZ} < \sigma_{\theta\theta}(30^\circ - \theta_{ZZ})/\sigma_{AC}$. Therefore, at the critical angle, the two ratios are identical:

$$\frac{\sigma_{\theta\theta}(\theta_C)}{\sigma_{ZZ}} = \frac{\sigma_{\theta\theta}(30^\circ - \theta_C)}{\sigma_{AC}}. \quad (S20)$$

And thus the fracture strength anisotropy factor is given as $A_\sigma = \sigma_{ZZ}/\sigma_{AC} = \sigma_{\theta\theta}(\theta_C)/\sigma_{\theta\theta}(30^\circ - \theta_C)$. This analysis, along with the measured $\theta_c = 18.2^\circ$, yields the strength anisotropy factor of graphene as $A_\sigma = 0.98$.

As a comparison, some theoretical results for fracture strength of graphene are summarized in Table S2. For some of the literature, the critical stress intensity factors for ZZ and AC cracks (K_{ZZ} and K_{AC}) are given. Since the critical stress intensity factor is linearly proportional to fracture strength, the anisotropic ratios for critical stress intensity factor and for fracture strength are identical (i.e., $A_\sigma = A_K$, where $A_K = K_{ZZ}/K_{AC}$). Therefore, they are both listed in Table S2.

Table S2. Summary of theoretical results on edge energy in literature.

Method	σ_{ZZ} or K_{ZZ}	σ_{AC} or K_{AC}	A_σ or A_K	Ref.
DFT	110 GPa	121 GPa	0.91	Ref. [13]
DFT	107.2 GPa	117.5 GPa	0.91	Ref. [14]
MD (SW)	129 GPa	142 GPa	0.91	Ref. [15]
MD (AIREBO)	3.97 MPa $\cdot \sqrt{m}$	4.04 MPa $\cdot \sqrt{m}$	0.98	Ref. [16]
MD (REBO)	3.05 MPa $\cdot \sqrt{m}$	3.38 MPa $\cdot \sqrt{m}$	0.90	Ref. [17]
MD (Tersoff)	3.8 MPa $\cdot \sqrt{m}$	4.1 MPa $\cdot \sqrt{m}$	0.93	Ref. [18]
MD (Tersoff)	4.0 MPa $\cdot \sqrt{m}$	4.2 MPa $\cdot \sqrt{m}$	0.95	Ref. [18]

Reference

- [1] S. Y. Park, H. C. Floresca, Y. J. Suh, and M. J. Kim, *Electron Microscopy Analyses of Natural and Highly Oriented Pyrolytic Graphites and the Mechanically Exfoliated Graphenes Produced from Them*, Carbon **48**, 797 (2010).
- [2] Y. Liu, A. Dobrinsky, and B. I. Yakobson, *Graphene Edge from Armchair to Zigzag: The Origins of Nanotube Chirality?*, Phys. Rev. Lett. **105**, 235502 (2010).
- [3] E. Gao, S. Z. Lin, Z. Qin, M. J. Buehler, X. Q. Feng, and Z. Xu, *Mechanical Exfoliation of Two-Dimensional Materials*, J. Mech. Phys. Solids **115**, 248 (2018).

- [4] E. Hamm, P. Reis, M. LeBlanc, B. Roman, and E. Cerda, *Tearing as a Test for Mechanical Characterization of Thin Adhesive Films*, *Nat. Mater.* **7**, 386 (2008).
- [5] H. Yin, H. J. Qi, F. Fan, T. Zhu, B. Wang, and Y. Wei, *Griffith Criterion for Brittle Fracture in Graphene*, *Nano Lett.* **15**, 1918 (2015).
- [6] C. K. Gan and D. J. Srolovitz, *First-Principles Study of Graphene Edge Properties and Flake Shapes*, *Phys. Rev. B* **81**, 125445 (2010).
- [7] P. Koskinen, S. Malola, and H. Häkkinen, *Self-Passivating Edge Reconstructions of Graphene*, *Phys. Rev. Lett.* **101**, 115502 (2008).
- [8] J. Gao, J. Yip, J. Zhao, B. I. Yakobson, and F. Ding, *Graphene Nucleation on Transition Metal Surface: Structure Transformation and Role of the Metal Step Edge*, *J. Am. Chem. Soc.* **133**, 5009 (2011).
- [9] K. Kim, V. I. Artyukhov, W. Regan, Y. Liu, M. F. Crommie, B. I. Yakobson, and A. Zettl, *Ripping Graphene: Preferred Directions*, *Nano Lett.* **12**, 293 (2012).
- [10] P. Zhang, L. Ma, F. Fan, Z. Zeng, C. Peng, P. E. Loya, Z. Liu, Y. Gong, J. Zhang, X. Zhang, P. M. Ajayan, T. Zhu, and J. Lou, *Fracture Toughness of Graphene*, *Nat. Commun.* **5**, 3782 (2014).
- [11] C. Y. Hui, A. T. Zehnder, and Y. K. Potdar, *Williams Meets von Karman: Mode Coupling and Nonlinearity in the Fracture of Thin Plates*, *Int. J. Fract.* **93**, 409 (1998).
- [12] X. Huang, H. Yang, A. C. T. van Duin, K. J. Hsia, and S. Zhang, *Chemomechanics Control of Tearing Paths in Graphene*, *Phys. Rev. B* **85**, 195453 (2012).
- [13] F. Liu, P. Ming, and J. Li, *Ab Initio Calculation of Ideal Strength and Phonon Instability of Graphene under Tension*, *Phys. Rev. B* **76**, 064120 (2007).
- [14] M. Xu, J. T. Paci, J. Oswald, and T. Belytschko, *A Constitutive Equation for Graphene Based on Density Functional Theory*, *Int. J. Solids Struct.* **49**, 2582 (2012).
- [15] M. Z. Hossain, T. Ahmed, B. Silverman, M. S. Khawaja, J. Calderon, A. Rutten, and S. Tse, *Anisotropic Toughness and Strength in Graphene and Its Atomistic Origin*, *J. Mech. Phys. Solids* **110**, 118 (2018).
- [16] M. A. N. Dewapriya and S. A. Meguid, *Tailoring Fracture Strength of Graphene*, *Comput. Mater. Sci.* **141**, 114 (2018).
- [17] B. Zhang, L. Mei, and H. Xiao, *Nanofracture in Graphene under Complex Mechanical Stresses*, *Appl. Phys. Lett.* **101**, (2012).
- [18] M. Q. Le and R. C. Batra, *Mode-I Stress Intensity Factor in Single Layer Graphene Sheets*, *Comput. Mater. Sci.* **118**, 251 (2016).

